Mon. Not. R. Astron. Soc. **385,** 453–467 (2008) doi:10.1111/j.1365-2966.2008.12859.x

# GRB 060607A: a gamma-ray burst with bright asynchronous early X-ray and optical emissions

Houri Ziaeepour,[1⋆] Stephen T. Holland,[2,3,4] Patricia T. Boyd,[5] Kim Page,[6] Samantha Oates,[1] Craig B. Markwardt,[5] Peter Mészáros,[7] Neil Gehrels,[2] Francis E. Marshall,[4] Jay Cummings[4] and Mike Goad[6]

[1]*Mullard Space Science Laboratory, Holmbury St Mary, Dorking, Surrey RH5 6NT*
[2]*Astrophysics Science Division, NASA Goddard Space Flight Center, Greenbelt, MD 20771, USA*
[3]*Universities Space Research Association, Suite 620, 10211 Winicopin Circle, Columbia, MD 21044-3431, USA*
[4]*CRESST, Room 260, Building 1, NASA Goddard Space Flight Center, Greenbelt, MD 20771, USA*
[5]*Laboratory for Astroparticle Physics, NASA Goddard Space Flight Center, Greenbelt, MD 20771, USA*
[6]*Department of Physics and Astronomy, University of Leicester, Leicester LE1 7RH*
[7]*Department of Astronomy and Astrophysics, Pennsylvania State University, 525 Davey Laboratory, University Park, PA 16802, USA*

Accepted 2007 December 14. Received 2007 December 14; in original form 2007 October 10

## ABSTRACT

The early optical emission of the moderately high redshift ($z = 3.08$) GRB 060607A shows a remarkable broad and strong peak with a rapid rise and a relatively slow power-law decay. It is not coincident with the strong early-time flares seen in the X-ray and gamma-ray energy bands. There is weak evidence for variability superposed on this dominant component in several optical bands that can be related to flares in high-energy bands. While for a small number of gamma-ray bursts (GRBs), well-sampled optical flares have been observed simultaneously with X-ray and gamma-ray pulses, GRB 060607A is one of the few cases where the early optical emission shows no significant evidence for correlation with the prompt emission. In this work we first report in detail the broad-band observations of this burst by *Swift*. Then by applying a simple model for the dynamics and the synchrotron radiation of a relativistic shock, we show that the dominant component of the early emissions in optical wavelengths has the same origin as the tail emission produced after the main gamma-ray activity. The most plausible explanation for the peak in the optical light curve seems to be the cooling of the prompt after the main collisions, shifting the characteristic synchrotron frequency to the optical bands. The fact that the early emission in X-ray does not show a steep decay, like what is observed in many other GRBs, is further evidence for slow cooling of the prompt shell within this GRB. It seems that the cooling process requires a steepening of the electron energy distribution and/or a break in this distribution at high energies. From simultaneous gamma-ray emission during the first flare, the behaviour of hardness ratio, and the lack of spectral features, we conclude that the X-ray flares are due to the collision of late shells rather than late reprocessing of the central engine activities. The sharp break in the X-ray light curve at few thousands of seconds after the trigger, is not observed in the infrared/optical/ultraviolet bands, and therefore cannot be a jet break. Either the X-ray break is due to a change in the spectrum of the accelerated electrons or the lack of an optical break is due to the presence of a related delayed response component.

**Key words:** shock waves – gamma-rays: bursts.

## 1 INTRODUCTION

GRB 060607A was a long, fairly hard gamma-ray burst (GRB) localized by the *Swift* Burst Alert Telescope (BAT) (Barthelmy et al. 2005) at $T_0 \simeq 05{:}12{:}13$ UT on 2006 June 7 (Ziaeepour et al. 2006).

⋆E-mail: hz@mssl.ucl.ac.uk

The *Swift* spacecraft rapidly slewed, directing the X-Ray Telescope (XRT) (Burrows et al. 2005) and the Ultraviolet and Optical Telescope (UVOT) (Roming et al. 2005) at the BAT position. The observations commenced at $T_0 + 63.6$ s after the BAT trigger in the optical/ultraviolet (UV) and $T_0 + 73.6$ s in the X-ray, providing broad-band spectral and high time resolution light curves in the X-ray, optical and UV. The X-ray light curve shows two bright flares, the first of which at $T_0 + 98$ s is also observed in the BAT energy range 15–300 keV. The second flare occurs at $T_0 + 260$ s and is marginally (if at all) detected by BAT (see Fig. 4). The optical emission is at first quite faint, then rises nearly 3 mag over a time-span of about 100 s. The peak in the optical is not simultaneous with the X-ray flares.

Historically, ground-based follow-up optical observations of GRBs usually started at least several minutes after the burst occurred, and it has not been unusual for optical observations to start several hours into the afterglow phase. Over the past few years fast-slewing robotic telescopes (see e.g. Boër 2001; Pérez-Ramírez et al. 2004; Vestrand et al. 2002; Akerlof et al. 2003; Covino et al. 2004) and the *Swift* mission (Gehrels et al. 2004) have made it possible to observe the first few minutes of optical emission from GRBs. In some cases, e.g. GRB 990123 (Akerlof et al. 1999), GRB 041219A (Vestrand et al. 2005), GRB 050820A (Vestrand et al. 2006), GRB 051109A, GRB 051111 (Yost et al. 2007), GRB 060124 (Romano et al. 2006), GRB 060418 (Molinari et al. 2007), GRB 060526 (Dai et al. 2007), GRB 060607A, GRB 061007 (Schady et al. 2007b), GRB 061121 (Page et al. 2007), GRB 070616 (Starling et al. 2007, 2008), the optical emission has been observed during the prompt gamma-ray emission. In the case of GRB 990123 there is no correlation between the structure of the gamma-ray light curve and the optical flux (Akerlof et al. 1999). If anything, there is an apparent anticorrelation, although the optical data are not well sampled. On the other hand, all the other bursts above show a correlation between the optical and gamma-ray fluxes. In the case of GRB 060124, although the optical flux slightly increases during the main peak at about 600 s, its relative rise is much smaller than the rise in gamma-ray and X-ray fluxes. In the case of GRB 060607A, clearly there is no correlation between the dominant component of the early optical and X-ray emissions. The optical flux arrived at its peak when the X-ray emission was decreasing. A similar behaviour was also observed in GRB 060418 (Molinari et al. 2007).

It is not yet clear how the prompt gamma-ray emission is related to the later emissions in the lower energy bands. *Swift* XRT observations have shown that the X-ray early emission of the most GRBs exhibit a very steep power-law decline with ($3 \lesssim \alpha \lesssim 5$, where the flux at time $t$ is $f_\nu \propto t^{-\alpha}$) decay within $T_0 + \lesssim 1000$ s (Butler et al. 2006; Nousek et al. 2006; O'Brien et al. 2006; Willingale et al. 2007)). This decay was expected to be caused by the high-latitude emission from the internal shocks that are driving the prompt high-energy emission, and therefore is not produced by the same mechanism that drives the late-time afterglow (e.g. Zhang & Kobayashi 2005; Liang et al. 2006), presumably the external shock with the interstellar medium (ISM) or wind. However, this rapid decay phase has not been observed in any optical early emission. Moreover, the high-latitude emission should satisfy a strict relation between $\alpha$ and the photon index $\beta$: $\alpha = 2 + \beta$ (Fenimore, Madras & Nayakshin 1996). This relation is however only satisfied in a small fraction of GRBs with a steeply decaying X-ray tail emission which also do not show significant spectral evolution (Zhang, Liang & Zhang 2007). The spectral evolution of the tail emission is another argument against high-latitude origin of the tail. Therefore, one can conclude that the high-latitude emission is not a dominant contributor in the tail emission. The fact that the light curves in different bands in general do not follow each other suggests that either multiple components should be involved (Kumar et al. 2007) and/or processes are chromatic and the emission evolves both in time and in energy. Therefore, one should expect various degrees of correlation between the light curves in the different energy bands depending on the internal properties of the system and its environment. GRB 060607A is a good example of how peculiar the relation between energy bands can be. The initial decay slope in X-ray is shallower than most bursts $\alpha \sim 1$, and the optical light curve shows a peak uncorrelated to the flares in gamma-ray and X-ray.

In this paper we focus on the early optical and X-ray emissions as observed by *Swift*'s UVOT and XRT instruments. The goal is to compare the multiband *Swift* data, with a simple relativistic shock and synchrotron emission model, and to try to reconstruct the history of events leading to the prompt and afterglow emission as observed by *Swift*. In Section 2, we describe the *Swift* observations. In Section 3, we present the time-variation analysis, and in Section 4, we discuss broad-band spectral variability during the early emission phase and give a qualitative interpretation of the data. In Section 5, we apply the model mentioned above to the data to interpret observations and to estimate some of the parameters. Finally, we summarize our results in Section 6. The theoretical model used in Section 5 is reviewed briefly in Appendix A. In Appendix B the conditions determining the reliability of the extrapolation of BAT light curve to the XRT energy band is discussed.

## 2 OBSERVATIONS

In this section we briefly report the result of the analysis of the BAT, XRT and UVOT data. Due to the peculiarity of the optical afterglow of this burst and its importance for the interpretation of the GRB, the UVOT data are discussed with more details.

### 2.1 BAT data

The BAT light curve showed a double-peaked structure with a duration of about 40 s (Tueller et al. 2006). The peak count rate was approximately 3000 count $s^{-1}$ (15–350 keV) at the time of the trigger. The mask-weighted light curve (Fig. 1) consists of two overlapping FRED-like peaks from $T_0 - 5$ to $T_0 + 40$ s. There is a second double-peaked structure between $T_0 + 95$ and $T_0 + 105$ s. $T_{90}$ (15–350 keV) is $100 \pm 5$ s (estimated error including systematics).

The time-averaged spectrum from $T_0 - 14.1$ to $T_0 + 104.5$ s is best fitted by a simple power-law model with a power-law index of $\Gamma = 1.45 \pm 0.07$. The fluence in the 15–150 keV band is $2.6 \pm 0.1 \times 10^{-6}$ erg $cm^{-2}$. The 1-s peak photon flux measured from $T_0 - 0.97$ s in the 15–150 keV band is $1.4 \pm 0.1$ ph $cm^{-2}$ $s^{-1}$. All the quoted errors are at the 90 per cent confidence level.

Using the spectroscopic redshift of this burst $z = 3.082$ reported by (Ledoux et al. 2006) and a cosmology with $\Omega_m = 0.3$, $\Omega_\Lambda = 0.7$ and $H_0 = 65$, we find $E_{iso}$ (1–1000 keV in the rest frame) to be $1.1 \times 10^{53}$ erg. This is based on an extrapolation of the BAT power-law fit into the corresponding observer energy band.

### 2.2 XRT data

Observations using the *Swift* XRT began 73.6 s after the trigger. It found a bright, variable, uncatalogued X-ray source (Page, Goad & Beardmore 2006). The XRT position enhanced by UVOT astrometry (Goad et al. 2007b) was at right ascension (RA) (J2000) =

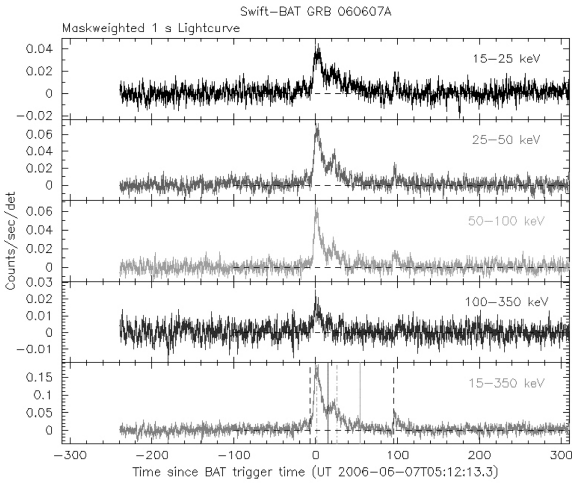


**Figure 1.** The mask-weighted light curves, at 1 s time resolution, for the BAT energy bands. The double FRED-like structure is visible at the start of all of the BAT light curves and a late peak is seen at approximately 100 s. Vertical lines: $T_{90}$ interval (dashed lines), $T_{50}$ interval (dash–dotted lines), slew interval (full lines).

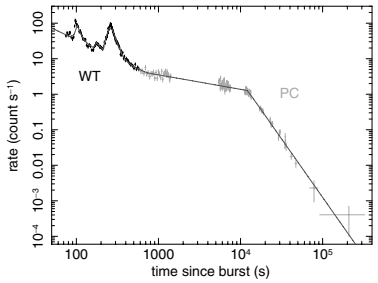


**Figure 2.** The XRT *X*-ray light curve (0.3–10 keV), WT (black), PC (grey). This plot includes all the XRT observations of GRB 060607A.

21:58:50.46 and declination (Dec.) (J2000) = −22:29:47.3, with an estimated uncertainty of 1.6 arcsec (90 per cent confidence radius).

The XRT light curve shows three flares peaking at approximately 97, 175 and 263 s after the BAT trigger. These flares are superposed on a decaying continuum with a decay index $\alpha_1 = 1.09 \pm 0.04$. At $714^{+88}_{-94}$ s after the BAT trigger the slope flattens, becoming $\alpha_2 = 0.41 \pm 0.03$. There is a second break at $12\,200^{+360}_{-350}$ s after which the decay becomes $\alpha_3 = 3.29^{+0.11}_{-0.1}$. The X-ray light curve of GRB 060607A is shown in Fig. 2.

### 2.3 UVOT data

The *Swift* UVOT observations began 63.6 s after the trigger with a 10 s settling mode exposure with the *V* filter, followed by finding chart exposures of 100 s with the White (160–650 nm) filter starting at $T_0 + 73.6$ s and then 400 s *V* filter (Oates, Blustin & Ziaeepour 2006). The settling exposure and each of the two finding chart exposures are taken in 'image and event' mode, so in addition to the full-frame integrated image, event-by-event data are also available at 11.0322 ms maximum time resolution.

A bright afterglow was detected in autonomous ground processing software, at RA = 21:58:50.40, Dec. = −22:29:46.7 (J2000) with a 1$\sigma$ error radius of approximately 0.5 arcsec. This position was 4.7 arcsec from the centre of the refined XRT error circle and is 0.95 arcsec from the XRT position enhanced by UVOT astrometry.

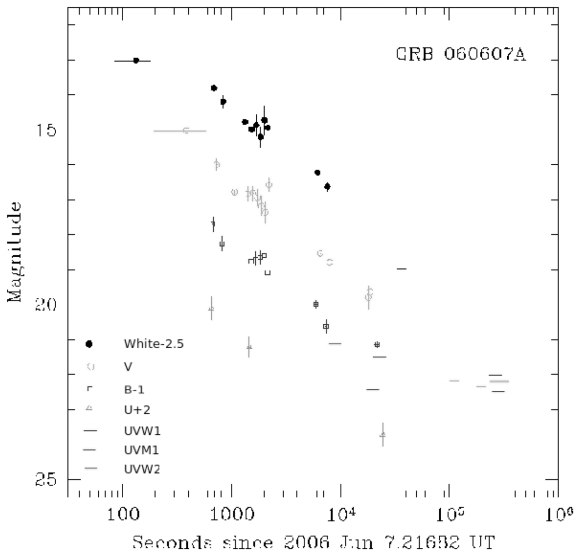


**Figure 3.** UVOT light curves in White, *V*, *B* and *U* extending out to where only 3$\sigma$ upper limits are seen. They are calculated from co-added exposures. The background was measured in annulus around the source position as explained in the text. The first imaging exposure from ∼73 to 172 s includes the rising part of the light curve, and therefore the rise of the optical flux is only observed in event-by-event data of the UVOT (see Fig. 4). Note also the episode of flattening, or possible rebrightening, between ∼1000 and 2000 s.

The estimated initial White magnitude in the finding chart image was 15.7 with a 1$\sigma$ error of ≈ 0.5 mag. The optical afterglow was also detected in White, *V*, *B* and *U* filters (Fig. 3). The non-detections in the UV bands are consistent with the spectroscopic redshift of $z = 3.082$ (Ledoux et al. 2006). We have also extracted 5-s binned light curves from event-by-event data to investigate the short time variability of the UVOT afterglow and to compare it to the XRT and BAT light curves (Fig. 4). Throughout this work, all the investigations of the UVOT data up to ∼600 s is based on this light curve.

We performed photometry on each UVOT exposure using a circular aperture with a radius of 2 arcsec centred on the position of the optical afterglow. This radius is approximately equal to the full width at half-maximum (FWHM) of the UVOT point spread function (PSF). The PSF varies with filter and with the temperature of the telescope, so we did not match the extraction aperture to the PSF for each exposure. The PSF FWHM, averaged over the temperature variations, ranges from 1.79 ± 0.05 arcsec for the *V* filter to 2.17 ± 0.03 arcsec for the UVW2 filter. The background was measured in a sky annulus of inner radius 17.5 arcsec and width 5 arcsec centred on the afterglow.

Aperture corrections were computed for each exposure to convert the 2-arcsec photometry to the standard aperture radii used to define UVOT's photometric zero-points (6 arcsec for *UBV* and 12 arcsec for the UV filters). Six isolated stars were used to compute the aperture correction for each exposure. The rms scatter in the mean aperture correction for a single exposure was typically ≈ 0.02 mag. The rms scatter for each exposure was added in quadrature to the statistical error in the 2 arcsec magnitude to obtain the total 1$\sigma$ error in each point.

Since the UVOT is a photon-counting device it is only able to record one photon per detector cell during each readout. This results in coincidence losses at high count rates. For very high count rates, corresponding to $V \lesssim 13.5$, these losses are significant and can

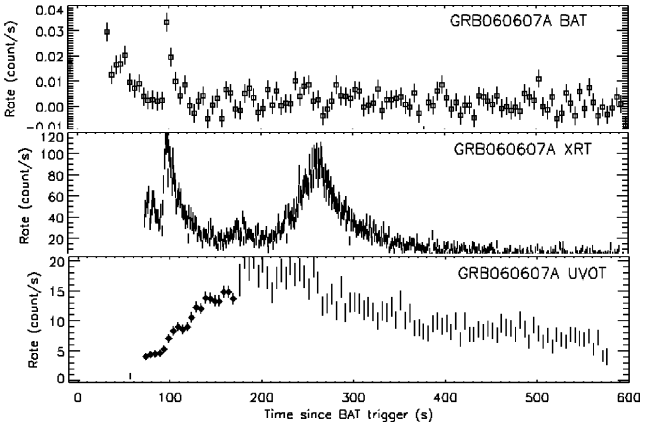


**Figure 4.** The light curves, at 5 s time resolution, for the BAT (upper), XRT (middle) and UVOT (bottom). The prompt double FRED-like structure as well as later spike at ∼100 s are visible in the BAT light curve. The XRT light curve shows probably a minor at the beginning of observations following by the flare at ∼100 s detected also by the BAT, then one minor flare at ∼170 s, and one major flare at ∼260 s. In the UVOT light curve circles correspond to the White filter and bars to *V* filter data points. The UVOT *V*-band count rates are weighted by a factor of ∼3. The optical light curve shows some variations at the time of flares, otherwise it is dominated by a continuous component peaking at ∼200 s.

dramatically affect the photometry, so coincidence loss corrections must be made. We have corrected all of our data for coincidence loss, although for most of the observations of the afterglow this correction is negligible.

The values quoted in Table 1 are not corrected for the expected Galactic reddening of $E(B-V) = 0.03 \pm 0.02$ mag (Schlegel, Finkbeiner & Davis 1998). This reddening corresponds to Galactic extinctions of $A_U = 0.15, A_B = 0.13$ and $A_V = 0.10$. The Galactic extinctions in the UVOT UV filters were calculated using the Milky Way extinction law from (Pei 1992). The UV extinctions are $A_{\rm UVW1} = 0.23, A_{\rm UVM2} = 0.29$ and $A_{\rm UVW2} = 0.21$ and $A_{\rm White} = 0.13$.

The afterglow was detected by UVOT from 63.6 s after the BAT trigger until it faded below detectability at approximately $2 \times 10^4$ s post-trigger. All significant detections as well as $3\sigma$ upper limits are listed in Table 1 and shown in Fig. 3.

There is not a unique way to fit light curves specially when they do not have a simple power-law behaviour. For the PROMPT telescope observations of GRB 060607A (Nysewander & Haislip 2006; Nysewander et al. 2007) authors have used a complex expression including absorption terms and power-law rising and falling terms around each of the features in the light curve. Here we are mainly interested in the origin of the dominant component of the optical light curves. Therefore, a simple power law separately fits on the rising and declining segments of the optical light curves is adequate. In Section 3 we also fit the optical light curve by adding a component proportional to the prompt gamma-ray to investigate the contribution of the prompt to optical emission.

For the rising section of the optical emission from ∼100 to 170 s only White filter observations are available. The light curve is fitted by a rising power law with $\alpha = 2.3 \pm 0.3$. The relatively large uncertainty is due to the varying components during flares in this time interval. The decay slopes are listed in Table 2. The weighted mean decay index is $\alpha = 0.9 \pm 0.06$ ($1\sigma$ error) for all times after ≈600 s after the BAT trigger. It is consistent with what is seen in other optical afterglows before the jet break occurs (Oates et al., in preparation).

**Table 1.** *Swift* UVOT photometry of GRB 060607A.

| Time + $T_0$ (s) | Filter | Exposure time (s) | Magnitude | Error |
|---|---|---|---|---|
| 385 | *V* | 387 | 15.03 | 0.04 |
| 728 | *V* | 19 | 16.00 | 0.16 |
| 1065 | *V* | 392 | 16.78 | 0.05 |
| 1413 | *V* | 19 | 16.83 | 0.22 |
| 1571 | *V* | 19 | 16.81 | 0.21 |
| 1724 | *V* | 19 | 16.95 | 0.23 |
| 1883 | *V* | 19 | 17.18 | 0.27 |
| 2041 | *V* | 19 | 17.36 | 0.29 |
| 2199 | *V* | 19 | 16.58 | 0.20 |
| 6555 | *V* | 195 | 18.53 | 0.17 |
| 7947 | *V* | 127 | 18.79 | 0.36 |
| 18 360 | *V* | 871 | 19.90 | 0.22 |
| 110 400 | *V* | 15 610 | >22.17 | – |
| 197 400 | *V* | 22 490 | >22.35 | – |
| 675 | *B* | 10 | 16.70 | 0.20 |
| 817 | *B* | 10 | 17.26 | 0.20 |
| 1513 | *B* | 19 | 17.77 | 0.20 |
| 1666 | *B* | 19 | 17.69 | 0.19 |
| 1825 | *B* | 19 | 17.65 | 0.20 |
| 1983 | *B* | 19 | 17.59 | 0.17 |
| 2136 | *B* | 19 | 18.08 | 0.28 |
| 5943 | *B* | 195 | 18.99 | 0.12 |
| 7372 | *B* | 193 | 19.62 | 0.20 |
| 21 710 | *B* | 2663 | 20.13 | 0.08 |
| 654 | *U* | 19 | 18.11 | 0.33 |
| 1455 | *U* | 117 | 19.21 | 0.28 |
| 24 580 | *U* | 5273 | 21.72 | 0.32 |
| 284 300 | *U* | 1808 | >21.65 | – |
| 132 | White | 97 | 15.52 | 0.06 |
| 686 | White | 10 | 16.31 | 0.24 |
| 833 | White | 10 | 16.70 | 0.18 |
| 1324 | White | 94 | 17.28 | 0.08 |
| 1529 | White | 10 | 17.49 | 0.20 |
| 1682 | White | 10 | 17.37 | 0.29 |
| 1840 | White | 10 | 17.71 | 0.29 |
| 1999 | White | 10 | 17.23 | 0.41 |
| 2152 | White | 10 | 17.45 | 0.51 |
| 6149 | White | 188 | 18.72 | 0.10 |
| 7578 | White | 195 | 19.13 | 0.13 |
| 36 560 | White | 747 | >21.48 | – |
| 24 180 | UVW1 | 4925 | >22.06 | – |
| 284 000 | UVW1 | 3376 | >22.00 | – |
| 23 710 | UVM2 | 3742 | >22.26 | – |
| 283 600 | UVM2 | 5539 | >22.64 | – |
| 9302 | UVW2 | 1423 | >21.16 | – |
| 284 700 | UVW2 | 7086 | >22.16 | – |

The first column shows the instant corresponding to the middle of the exposure since trigger time.

The decay slope is the same before and after the fluctuation in the light curve between 1000 and 2000 s. This feature was also observed by the PROMPT telescope (Nysewander et al. 2007) and by the REM telescope (Molinari et al. 2007), and is probably the optical emission from a weak flare at about 1000 s after trigger, see Fig. 2. Another feature was observed by the PROMPT telescope between ∼3000 and ∼4000 s. However, a gap in the *Swift* data from ∼1500 to 5000 s does not allow to see if it is related to an X-ray flare.

There is also a faint feature in the UVOT light curve that at first sight can be considered as noise: a double peak at the time of maximum flux. This feature is independently observed also by the

**Table 2.** *Swift* UVOT decay slopes of GRB 060607A.

| Filter | $\alpha$ | Error ($1\sigma$) | $\chi^2$/(d.o.f.) |
|---|---|---|---|
| *V* | 1.21 | 0.03 | 72.29/11 |
| *B* | 0.88 | 0.04 | 12.47/8 |
| *U* | 0.88 | 0.11 | 0.61/1 |
| White | 0.77 | 0.02 | 17.68/9 |

PROMPT (Nysewander et al. 2007) in *B* and by the REM (Molinari et al. 2007) telescopes in *H* filter, and therefore most probably is real. It can be related to the flare at $T_0 + 179$ s.

## 3 ANALYSIS OF TIME VARIABILITY

The brightness of the early X-ray and optical emissions of GRB 060607A together with good time resolution of the *Swift* onboard instruments permit the investigation of the relation between various features observed in different energy bands. This is very important for identifying the related physical processes and their modelling. In this section we investigate the correlation between features.

As mentioned in the previous sections, it is very clear that a fast-varying component is superposed on the dominant continuous component of the optical emission. In order to determine the contribution of this fast-varying component to the optical afterglow during early UVOT observations, we performed an analysis similar to that of Vestrand et al. (2005). We assumed that the UVOT light curve could be represented by a component proportional to the gamma-ray component in the same time interval:

$$F_{\rm p}(t) = C_{\rm p} F_\gamma(t) \tag{1}$$

and a continuous component of the form

$$F_{\rm a}(t) = C_{\rm a}\left(\frac{t-t_0}{t_0}\right)^{-s} \exp\left(\frac{-\tau}{t-t_0}\right)\Theta(t-t_0), \tag{2}$$

where $t_0$ is an arbitrary initial time, $\tau$ is the time-scale for the rise of the optical emission, $s$ is the power-law decay index and $C_{\rm p}$ is the ratio of the UVOT fast-varying component in White filter (the only filter with simultaneous BAT detection) to the BAT 15–150 keV flux, and $C_{\rm a}$ is the amplitude of the continuous component of the optical emission. The step function $\Theta$ is added to restrict this equation to $t \geqslant t_0$.

Our best fit is shown in Fig. 5. The best fit has $t_0 = 37.9 \pm 2.3$ s, $\tau = 209 \pm 5$ s. The power-law index has been fixed to $s = 2$. The ratio of the fast-varying component to the continuous afterglow in the UVOT data is $C_{\rm p}/C_{\rm a} = (6.25 \pm 8.20) \times 10^{-2}$. This suggests that the fast-varying optical emission makes a small, if not negligible, contribution to the observed optical light at the time of the flares. This is in contrast to what was found for some of other GRBs with simultaneous gamma-ray, X-ray and optical observations: GRB 041219A (Vestrand et al. 2002), GRB 050820A (Vestrand et al. 2005), GRB 060526 (Dai et al. 2007), GRB 061121 (Page et al. 2007), where the prompt/flare component of the optical light makes a significant contribution to the total optical light. The possible reason can be the fact that for these bursts BAT had triggered on a faint precursor that produced a faint continuous emission before the occurrence of the main gamma-ray peak. In the case of GRB 060607A the main peak was at trigger time and had a significant tail emission. The time varying component here is due to fainter flares at later time, and therefore less significant than the remnant of the prompt emission.

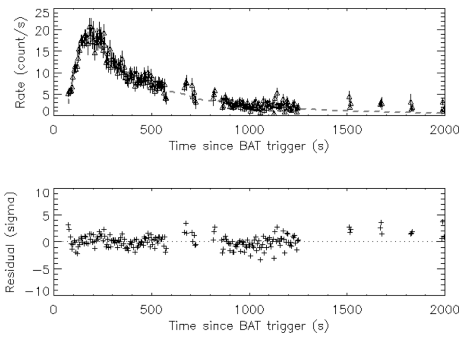


**Figure 5.** The UVOT White and *V*-band data are fitted by the two-component model (dashed line) described in Section 3. The data from the two filters have been arbitrarily shifted so that they are aligned.

To see whether the X-ray and the optical light curves correlate or more precisely if there is any trace of the flares in the UVOT light curve, we removed the smooth component of the rising section in White filter using the Savitzky–Golay smoothing algorithm (Savitzky & Golay 1964), and correlated the residuals with the XRT light curve in 0.3–10 keV. The feature in the rising part of the White filter light curve correlates with the flare at $T_0 + 98$ s in the XRT with a lag of $\sim$5 s. The trace of the flare at $T_0 + 260$ s is less evident. As mentioned in Section 2.3 there is a break in the *V*-band light curve (Fig. 4) with a lag of $\sim$5 s around this time, but it is less significant than the first flare.

As for the common gamma-ray and X-ray flares, Fig. 4 shows that they are very close and correlate with each other with a lag of $\lesssim$1 s with 15–300 keV BAT band. There is also a weak evidence of a peak close to $T_0 + 260$ s and the correlation between this section of the BAT and XRT light curves gives a lag of $\sim 12 \pm 5$ s.

## 4 BROAD-BAND SPECTRAL AND LIGHT CURVES VARIABILITY

We fit the X-ray spectra using XSPEC-12 (Arnaud 1996). The model used was a power-law spectrum with variable hydrogen column density in the host galaxy and a Galactic hydrogen column density fixed at $N_{\rm H}^{\rm MW} = 2.67 \times 10^{20}\,{\rm cm}^{-2}$. We adopted a redshift of $z = 3.082$ for this burst and its host galaxy. The photon-counting data before the break – mainly the shallow slope regime – are well fitted by a single power law with $\Gamma = 1.59 \pm 0.06$ and an excess $N_{\rm H}$ of $5.7^{+2.9}_{-2.7} \times 10^{21}\,{\rm cm}^{-2}$ at the redshift of the source. After the break the spectral slope is $\Gamma = 1.73 \pm 0.08$. There is no evidence for a change in the column density across the break at $\sim$12 200 s. The brightness of the X-ray afterglow permits the spectrum to be determined before, during and after flares. From Fig. 2 it is clear that strong flares overlap the continuum X-ray emission. For this reason we have selected four intervals of 10 s during which the flares or the continuum are expected to be the dominant contributors to the X-ray light curve. The duration was selected such that there were enough events at later times – smaller fluxes – to obtain a statistically significant spectrum index and $N_{\rm H}$. The first and the last intervals belong to the continuum in the region usually called tail emission. The last interval was positioned to be as far as possible from the transition region between tail emission and the shallow slope regime. The other two intervals are positioned near the peaks of the main flares. They allow to measure spectral differences between maximally different features of the light curve. The results are summarized in Table 3.

**Table 3.** Spectral fits to the X-ray data.

| XRT flares | Time + $T_0$ (s) | $\Gamma$ | $N_{\rm H}$ ($10^{22}$ cm$^{-2}$) |
|---|---|---|---|
| Before first flare | 79.5–89.5 | $2.09^{+0.26}_{-0.23}$ | $1.1^{+1.2}_{-0.9}$ |
| Peak first flare | 91.5–101.5 | $1.34 \pm 0.13$ | $< 0.92$ |
| Peak second flare | 257.5–267.5 | $1.60^{+0.13}_{-0.12}$ | $1.1^{+1.0}_{-0.8}$ |
| After second flare | 394.5–404.5 | $2.00^{+0.42}_{-0.45}$ | $< 0.76$ |

$N_{\rm H}$ are at the redshift of the source $z = 3.082$. Galactic $N_{\rm H}$ is $2.6 \pm 0.05 \times 10^{20}$ cm$^{-2}$.

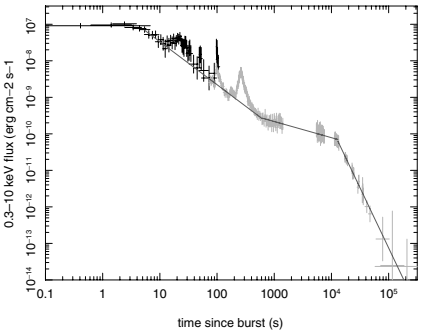


**Figure 6.** The BAT light curve (black) extrapolated into the XRT band using the mean of the BAT and pre-flare WT spectra, and the XRT light curve (grey). The red curve shows the fit on the continuum component of the light curve from $T_0 + 5.41$ on. For $T_0 + 5.41$ to $T_0 + 635.96$ the slope is $\alpha = 1.17 \pm 0.04$, consistent at $1\sigma$ level with $\alpha_1$ in Section 2.2. For the other segments the results are the same as what is reported in Section 2.2.

We discuss them later in this section along with the evolution of the X-ray hardness ratio.

There are coincident BAT and XRT flares at approximately 100 s, so we performed a joint spectral fit to the BAT and XRT data during the flare. The best fit is obtained using the same model as described above for the XRT-only fits. It has $\Gamma = 1.63 \pm 0.05$ and $N_{\rm H}$ is consistent with the value that was determined using only the XRT data. Changing the model to a broken power law or a cut-off power law does not improve the fit. The joint BAT + XRT spectral slope is consistent with what was found for the XRT data, so we conclude that the X-ray flare is an extension of the flare seen in the gamma-rays. Fig. 6 shows the BAT light curve extrapolated to the XRT band using the mean of the BAT and pre-flare WT spectra, along with the XRT light curve. In addition, it shows power-law fits on the different segments of the continuum component of the light curve. There is a smooth power-law decaying component, from the time at which the first gamma-ray peak begins to fall at $\sim T_0 + 5$ s, until the end of the last major flare in X-ray at $\sim T_0 + 700$ s. The decay slope of this segment is $\sim$1.17. Flares, in both BAT and XRT, are superposed on this continuum. It is evident that flares observed by both instruments are in close relation, and therefore X-ray flares have the same origin as the prompt gamma-ray emission, presumably the internal shocks. As mentioned in Section 3, the correlation of XRT and UVOT light curves shows an excess of optical emission during the flares. In conclusion, the late flares are simultaneously observed by all instrument onboard of the *Swift*.

A confirmation of the hypothesis that flares have the same origin as the prompt gamma-ray can come from a direct comparison of their emission properties. There is a well-known relation between the width of autocorrelation of peaks and the energy bands first discovered by Fenimore et al. (1995) – the lower the energy band, the larger the width of the autocorrelation of a peak. We tested this relation for the BAT peaks and for the flare at $\sim T_0 + 98$ s observed by both BAT and XRT. In all cases peaks have a wider autocorrelation for lower energy bands. Another suggested relation is the proportionality of the waiting time during a quiescent period and subsequent burst of radiation, evidence for a sort of accumulation of energy behaviour (Ramirez-Ruiz & Merloni 2001; Ramirez-Ruiz, Merloni & Rees 2001; Nakar & Piran 2002). We cannot confirm this relation for GRB 060607A. In fact, it seems that the amplitude of fainter peaks following the main peak at trigger time decreases according to a power law, somehow shallower than continuum emission, regardless of the quiescent interval between them, see Fig. 6.

In order to estimate the shortest variability time-scale of the prompt and flares we use their Fourier transform and autocorrelation. The shortest variation time-scale distinguishable from a white noise for the prompt gamma-ray from $T_0 - 5$ to $T_0 + 95$ s is $\sim 2.5 \pm 1$ s in all bands. For the flare (peak) at $\sim T_0 + 98$ s, the minimum variability distinguishable from noise is close to the main peaks, $\sim 3 \pm 1$ s, using the total light curve for the BAT in 15–300 keV and for the XRT data in 0.3–10 keV. The minimum variability of the flare at $\sim T_0 + 260$ s is $\sim 7 \pm 5$ s, longer than previous peaks. Variation in the emission can be due to the inhomogeneity in the shells and/or their limited size. In this case one expects that with the expansion of the fireball or what rests from it, the density variation dilutes. Therefore, what we expect is an increasing minimum time variability with time, which is exactly what we are observing. However, as with expansion the signal becomes fainter and the variations become more difficult to observe, the increase in minimum variability scales is a consequence of both effects.

As the speed of the passage of the shock front through a shell is limited to the speed of light, these time-scales can be translated to the distance travelled by a relativistic ejecta. Therefore, they constrain the initial size and/or variability scale of the fireball, and the distance to the central engine to $\gtrsim 3 \times 10^{10}$ cm in the rest frame of the engine. This is consistent with the estimation of the model explained in Appendix A and applied to the data in Section 5. The time-scales are also another confirmation of the same origin for the prompt emission and flares seen in X-ray and optical bands. The increasing time-scale of variations is consistent with the expansion of what rests from the prompt shell (fireball) after internal shocks and its coalescence with other shells.

As for the continuum emission, there is no evidence of a steep initial decline as would be expected from a high-latitude emission. One possibility is that the external shock phase with ISM/surrounding material began very early and smeared the high-latitude emission. Another possibility is that the continuous emission and the preceding peaks in the prompt emission have the same origin; with the continuous emission due to the decaying tail of the emission from the prompt shell after its main collision. As explained earlier in this section, a power law fits the extrapolated BAT light curve to the XRT energy band. The smoothness of the joint light curve is a likely evidence that the initial smooth, sometimes very steep decay observed in the X-ray light curve of many GRBs is directly related to the prompt emission and hence the term *tail emission* is a correct expression for this regime. As for the physical processes involved, it is possible that the magnetic field in the coalesced shells has a relatively long lifetime and electrons are accelerated and support a synchrotron emission at a lower rate well after the end of the collision between shells. See also Section 5 for more details. There is however a caveat in this argument. The extrapolation of the BAT light curve to the XRT uses the average spectrum slope observed by these instruments in their corresponding bands. Therefore, the smoothness of the joint light curve may be due to the way it is

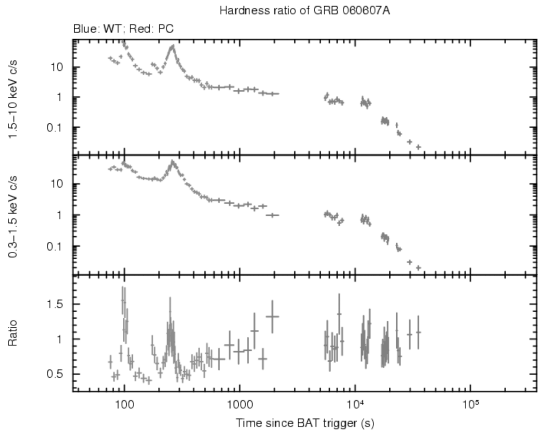


**Figure 7.** The upper and middle panels show the count rate measured by the XRT in 1.5–10 and 0.3–1.5 keV, respectively. The lower panel shows the evolution of the hardness ratio, the ratio of the flux measured in the 1.5–10 keV band to that measured in the 0.3–1.5 keV band. Darker points are observations in WT (window timing) mode and lighters in PC (pulse counting) mode.

calculated, thus the argument about common origin of the prompt and tail emission becomes doubtful. None the less, we show in Appendix B that if the time evolution of the BAT spectrum index is taken into account, it is highly improbable to obtain such a smooth common light curve due to averaging or by chance, and one should observe a deviation between extrapolated BAT light curve and what is observed by the XRT if there is not an intrinsic relation between the prompt and the tail emissions.

Fig. 7 shows the evolution of the X-ray hardness ratio: $\mathrm{HR_X} \equiv C(1.5\text{–}10\,\mathrm{keV})/C(0.3\text{–}1.5\,\mathrm{keV})$, where $C$ is the count rate uncorrected for the absorption. Both of the X-ray flares are significantly harder than the underlying decay, consistent with the spectral indices reported in Table 3. Moreover, comparing the spectral index of the spectrum of the first and the last time intervals reported in this table, and their hardness ration shown in Fig. 7, it seems there is no evidence for large spectral evolution in the continuum emission until entering to the shallow slope regime. The hardness ratio during each flare tracks the luminosity; that is, the hardness increases as the flare brightens, and decreases as the flare fades. Another interesting observation from this plot is a gradual rise of the hardness ratio from the beginning of the shallow regime to a roughly constant plateau that does not decline even after the sharp break at $\sim 1.2 \times 10^4$ s. If the break was achromatic such a behaviour was expected; however, the break is not achromatic. It can be due to a decrease in the number of emitters – accelerated electrons – and hardening of their spectrum, and/or a stronger magnetic field. In Section 5 we discuss these issues more in details.

The fluence in gamma-rays (15–150 keV) during the first pulse ($T_0 - 24$ to $+12$ s) is $(1.38 \pm 0.05) \times 10^{-6}$ erg cm$^{-2}$ while the corresponding fluence between 24 and 102 s is $(1.22 \pm 0.05) \times 10^{-6}$ erg cm$^{-2}$. There is no flux in the 15–150 keV band after 102 s. Therefore, unlike the first flare the second XRT flare has no (or a marginal) BAT counterpart. This suggests that the two XRT flares are produced by distinct shells colliding with the remnant of the prompt shell.

It seems that both main flares were preceded by fainter but harder flares, see Fig. 6. This repetition can be explained if two late shells successively pass through the remnant of the prompt shell. In this case the observed emission is the tomography of the prompt. The small and large successive flares can be the result of collision between the late shell, slower shocked material and a leftover unshocked material from the prompt shock with a larger Lorentz factor that moves ahead of the first component. A similar configuration of flares is also visible in the X-ray light curve of GRB 070107 (Stamatikos et al. 2007). Assuming that the late shells have roughly the same dynamical properties – Lorentz factor, density, etc. – the softness of the second flare could be due to the expansion and slowdown of the unshocked remnant. The expansion of the late shell can also be in part responsible for the softer radiation during collision, which in this interpretation had necessarily happened at larger distances from the central engine.

**Table 4.** The closure relationships for various assumptions about the location of the cooling frequency and the nature of the circumburst medium. A closure value of zero indicates agreement with the predictions of each case.

| Model | Environment | Closure | Value |
|---|---|---|---|
| $\nu_X < \nu_c$ | ISM | $\alpha - 3/2\beta$ | $-0.13$ |
| | Wind | $\alpha - 3/2\beta + 1/2$ | $+0.63$ |
| $\nu_c < \nu_X$ | ISM | $\alpha - 3/2\beta - 1/2$ | $-0.37$ |
| | Wind | $\alpha - 3/2\beta - 1/2$ | $-0.37$ |

The observed X-ray decay slope after flares and up to $\sim T_0 + 600$ s when the shallow regime began, is $\alpha_X = 1.09 \pm 0.04$. The spectral index of the X-rays in the same interval is $\beta_X = \Gamma - 1 = 0.64 \pm 0.07$. If the emission in this interval is due to an external shock with ISM/circumburst material, the closure relationships can be used to determine the density distribution. We consider two cases: a constant-density circumburst medium and a wind-stratified circumburst medium. The closure values are given in Table 4. The case that gives a closure closest to zero is one with a constant-density medium and the cooling frequency above the X-ray band at 600 s. Further evidence for the cooling break being above the X-ray band in this time interval is that the optical decay has a slope of $\alpha_{opt} = 0.9 \pm 0.06$, close to the X-ray slope at $1\sigma$ and consistent with it at $2\sigma$ level. If this scenario is correct, the electron index is predicted to be $q = p + 1 \sim 3.5$, consistent with what is seen in many other GRBs (Shen, Kumar & Robinson 2006). The optical decay does not change between $\sim$600 and 20 000 s after the BAT trigger, so the cooling break must be above optical frequencies during this period.

As for what we can learn about the gas and dust content of the host galaxy of GRB 060607A, the fitted neutral hydrogen column density in the host along the line of sight to the burst is consistent with $N_H = 1.6 \times 10^{22}$ cm$^{-2}$, which implies a high extinction in the host galaxy. (Predehl & Schmitt 1995) find $N_H = (1.79 \times 10^{21})\, A_V$ for the conversion between hydrogen column density and extinction in the Milky Way. If this relationship holds for the host galaxy, then $A_V = 8.9$ mag in the host. While the optical data do not rule out such a high extinction there is no evidence for it either. If we assume an $N_H/A_V$ ratio like that in the Small Magellanic Cloud (SMC) of $N_H = (15.4 \times 10^{21})\, A_V$ (from equation 2 and table 2 of (Pei 1992) then $A_V$ in the host is 1.0 mag.

Gas-to-dust ratios similar to that of the SMC have been observed for several GRB host galaxies, such as GRB 000301C (Jensen et al. 2001), GRB 000926 (Fynbo et al. 2001), GRB 020124 (Hjorth et al. 2003) and XRF 050416A (Holland et al. 2007), see also (Schlegel, Finkbeiner & Davis 1998; Kann, Klose & Zeh 2006). Detailed investigation of seven *Swift* bursts (Schady et al. 2007a) shows that

only in one case the extinction is best modelled by Milky Way gas-to-dust ratio, and for other cases the extinction is more similar to SMC. Giving the fact that GRB 060607A was observed in all the rest frame bands redder than Ly$\alpha$ suggests that it may be reasonable to assume that the host galaxy of GRB 060607A has a high gas-to-dust ratio. This could indicate that star formation in the host is fairly recent and there has not been enough time for large amounts of gas to be processed into dust. Alternately, a high ratio could be indicative of dust destruction in the vicinity of the progenitor by the burst itself (Waxman & Draine 2000; Perna, Lazzati & Fiore 2003; Watson et al. 2007).

There is no evidence for a jet break in the optical light curve out to ∼20 000 s after the BAT trigger. This, and the isotropic energy of the burst, can be used to put a lower limit on the opening angle of the jet, and the total gamma-ray energy of the burst (Rhoads 1999; Sari et al. 1999; Frail et al. 2001). Assuming a single jet, the lower limit of the jet opening angle for GRB 060707A is

$$\theta_j \geqslant 0.161\left(\frac{t_j}{z+1}\right)^{3/8}\left(\frac{n\eta_\gamma}{E_{\rm iso}}\right)^{1/8} = 0.025\left(\frac{\eta_\gamma}{0.2}\right)^{1/8}\left(\frac{n}{0.1}\right)^{1/8}\ {\rm rad}, \quad (3)$$

where $\eta_\gamma$ is the efficiency of converting energy in the ejecta into gamma-rays, and $n$ is the particle density in cm$^{-3}$. The corresponding energy in gamma-rays, using $E_{\rm iso}$ obtained in Section 2.1 in the rest frame of the engine and corrected for the beaming is $E_\gamma \geqslant 3.3 \times 10^{49}$ erg.

## 5 MODELLING

In this section we apply a reformulation of the internal/external shock model for the prompt and afterglow to the data in order to estimate some of the parameters of the burst. This formulation is based on a simplified ultrarelativistic radiative shock model with one synchrotron emitting shocked layer but more detailed parametrization of the physical processes and their time variation (Ziaeepour, in preparation). A summary of the model and its main results are given in Appendix A.

### 5.1 Methodology

A major difficulty in understanding the behaviour of GRBs is that the main ingredients of the shock, i.e. the electric and magnetic fields, and the distribution of electrons varies in a complex manner with time during the evolution of the microphysics and the dynamics of the shock (Bednarz & Ostrowski 1996; Waxman & Draine 2000; Wiersma & Achterberg 2004; Reville, Kirk & Duffy 2006; Rieger, Bosch-Ramon & Duffy 2006). The commonly used power-law parametrization with constant coefficients and indexes is not able to explain the complex behaviour of quantities and thereby the synchrotron emission. Adding the microphysics of the shock to the formulation of the shock dynamic is also too difficult as in most cases there is no analytical expression for their evolution, or for the evolution of the electric and magnetic fields or distribution of electrons. As we will explain in more details, we found that the best way to estimate parameters and to explain the behaviour of the light curves is to divide them into subregimes that can be explained separately by a simple power-law parametrization. On the other hand, this simplified model still requires 12 parameters and thus fitting such a complex model to the data is not trivial, even after subdividing it into separate regimes. The degeneracy between parameters and the instability of numerical fitting can lead to confusing results. Moreover, at the current level of our knowledge about GRBs and the precision of available data, even a rough estimation of parameters permit a better understanding of the nature of these elusive objects and can be considered as an achievement. Therefore, rather than fitting the data, we determine the predictions of the model through numerical simulations with prefixed parameters. Then, we estimate the set(s) of parameters that best reproduce the behaviour of the data.

### 5.2 Modelling and interpretation of the BAT data

To interpret the light curves of the GRB 060607A, we begin with the hardness ratios of the BAT bands. The hardness ratios of the first main peak are shown in Fig. 8. The initial rapid rise is consistent with an exponential growing to a saturated value of $\epsilon_{\rm e}$ and $\epsilon_B$, respectively, of the fraction of kinetic energy transferred to accelerated electrons and to magnetic field. This is also in accordance with simulations of the formation of magnetic field (Yang, Arons & Langdon 1994; Wiersma & Achterberg 2004), parallel instabilities (Reville et al. 2006) in the relativistic shocks, and acceleration of particles in

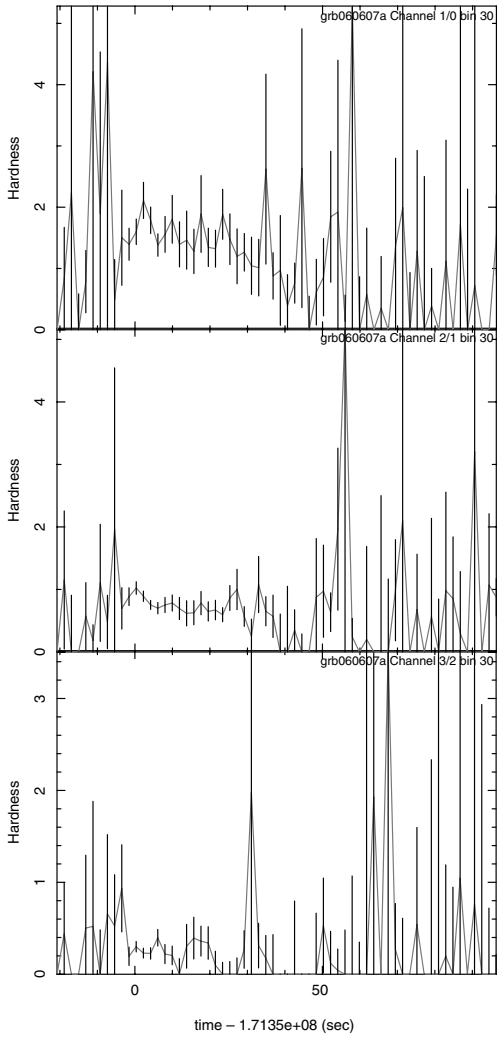


**Figure 8.** Hardness ratios of the main peak. From top to bottom: $\mathrm{HR}_{10} \equiv C(25\text{–}50\,\mathrm{keV})/C(15\text{–}25\,\mathrm{keV})$, $\mathrm{HR}_{21} \equiv C(50\text{–}100\,\mathrm{keV})/C(25\text{–}50\,\mathrm{keV})$ and $\mathrm{HR}_{32} \equiv C(100\text{–}300\,\mathrm{keV})/C(50\text{–}100\,\mathrm{keV})$. For calculation of the ratio data from the 64-ms binned light curve are used and rebinned by a factor of 30.

a Fermi process (Bednarz & Ostrowski 1996; Rieger et al. 2006).[1] After this transient time, fields settle into a quasi-stationary regime in which they decline according to a power law. Comparison with simulations show that for this burst $\eta \equiv 2\,\alpha_e + \alpha_B/2 \sim 3.5 \pm 0.5$ for a power-law electron number distribution index $q \sim 3.5 \pm 0.5$, where $\alpha_e$ and $\alpha_B$ are time/radius dependence of $\epsilon_e$ and $\epsilon_B$, respectively. The value of $q \sim 3.5$ (or equivalently $p \sim 2.5$) is close to $p \sim 2.2$–2.3, the *universal* value suggested by simulations (Kirk et al. 2000; Achterberg et al. 2001). On the other hand, the distribution of $p$ obtained from the observations of GRBs and other relativistic sources does not show a universal average and has a relatively large deviation around the mean value (Shen et al. 2006). This can be the evidence for more complex outflow behaviour, such as, a complex geometry of the magnetic field and shock, plasma currents and turbulence, non-Fermi acceleration mechanisms or dominance of the Poynting flux. In conclusion, although the $p$ value obtained here is typical, it cannot give more information about the underlying processes. The estimated value of characteristic synchrotron energy of the electrons with minimum Lorentz factor $\Gamma$ is $\mathcal{E}_m \equiv h\nu_m \sim 12(1+z) \sim 50$ keV in the rest frame of the engine.

These estimations are based on the hardness ratios $HR_{10}$ and $HR_{21}$. The highest energy band hardness $HR_{32} \equiv C(100$–$300\,\mathrm{keV})/C(50$–$100\,\mathrm{keV})$ is much noisier than $HR_{10}$ and $HR_{21}$. However, it seems that the electron spectrum should be much steeper to explain the observed low value of $HR_{32} \sim 0.4$ in place of the expected value of $\sim$0.65 from simulations for $q$ and $\eta$ as mentioned above. We interpret this as an upper limit cut-off or steepening in the electron distribution. Simulations of electron acceleration by shocks (Amano & Hoshino 2007) also confirm a steeper distribution at high energies. A change in the spectrum of electrons has been also invoked as an explanation for the chromatic break in the X-ray and optical afterglows (Wei & Lu 2002; Misra et al. 2007). The observation of such a break/steepening in electron energy distribution during the prompt emission, when the shock is much stronger, shows that the popular assumption of a power-law distribution is too simplistic and far from reality. The estimated range of parameters includes both uncertainties and degeneracy between them. The initial (maximum) value of the hardness ratios depends mainly on $q$, their decreasing rate depends on $\eta$ and coefficient $F$ defined in (A3), and there is a significant degeneracy between these quantities.

From the slope of the hardness ratios in the quasi-steady regime and the lag between the BAT energy bands, we can estimate the coefficient $F$ and the distance to the central engine. The lags between the BAT bands are presented in Table 5. Considering the peak time after the initial rise as the beginning of the power-law decline regime for $\epsilon_e$ and $\epsilon_B$, and by comparing lags with simulations, we conclude that $F \sim 12$–$18$, $\Delta\epsilon_{02} \sim 6 \times 10^{-6}$ and $\Delta\epsilon_{12} \sim 3 \times 10^{-6}$, where $\Delta\epsilon_{ij}$ is the difference between $\epsilon$ defined in equation (A3) at peak time for bands $i$ and $j$. Including uncertainties both in data and comparison with simulations, we estimate the initial distance to the central engine as $r_0 \sim 10^{12}$ cm. This is roughly in the middle of the distance range predicted for the internal shocks (Rees & Mészáros 1994).[2]

Knowing $F$ and $r_0$, we can also estimate the relative Lorentz factor of the shells. In the radiative shock model assumed here colliding shells coalesce. Therefore, at the end of the shock, $\gamma \to 1$. Using equation (A3), $\gamma_0^2 \approx 1 + F\epsilon_f$ where $\epsilon_f$ corresponds to the value of $\epsilon$ at the end of the coalescence. It is not very evident what time should be used to determine $\epsilon_f$, because substructures/overlapping peaks can be due to separate shells or from density inhomogeneities in the same shell. Moreover, the limited sensitivity of the BAT can smear the real collision time. None the less, if we assume that the detected duration of the peaks corresponds to the main part of the collision, an estimation of $\gamma_0 \sim 1.5$–$3.5$ for overlapping peaks from $\sim T_0 - 5$ to $\sim T_0 + 40$ s can be made. This includes uncertainties in the parameters and the duration of the collision. The bulk Lorentz factor of the ejecta however cannot be determined from the prompt without knowing all the parameters such as the density of shells, magnetic fields, etc. The reason is the fact that the physics of shock depends only on the relative Lorentz factor, and the detected radiation is just boosted by the bulk Lorentz factor to the observed energies. Other BAT peaks are too weak to permit a detailed analysis of their corresponding shock.

**Table 5.** BAT lags.

| Band | Lag (ms), entire burst |
|---|---|
| 0–2 | $621.90 \pm 57.0$ |
| 1–2 | $252.18 \pm 25.7$ |
| 3–2 | $-556.73 \pm 57.0$ |

### 5.3 Modelling and interpretation of the XRT data

If we neglect flares that are superimposed on the early XRT light curve shown in Fig. 2, the power-law component from $\sim T_0 + 73$ to $\sim T_0 + 700$ s has a slope of $\alpha_1 \sim 1.09$ and spectrum index of $\beta_1 \sim 0.64$. These indices do not satisfy the relation $\alpha_1 = \beta_1 + 2$ for high-latitude emission. Therefore, we interpret this section of the X-ray light curve as the tail emission from energy dissipation in the prompt shell after the termination of the coalescence. Investigation of the hardness ratio of the X-ray bands $C(1.5$–$10\,\mathrm{keV})/C(0.3$–$1.5\,\mathrm{keV})$ shows that at this time the ejecta has significantly cooled, consistent with the results of Section 4. In fact, we can go further and determine $\mathcal{E}_m$ at the beginning of the observations after *Swift* slewed to this burst.

Assuming synchrotron radiation as the source of the observed X-ray, according to our model, $\mathcal{E}_m$ evolves as[3]

$$\mathcal{E}_m(r) = \mathcal{E}_m(r_0)\left(\frac{r}{r_0}\right)^{-\eta}\left(\frac{\gamma^2}{\gamma_0^2}\right)^{5/4}. \quad (4)$$

After the coalescence of the two shells $\gamma = 1$, and therefore at $\sim T_0 + 73/(z+1)$ s in the source frame when the coalescence of the shells has been already finished, the second term in equation (4) is fixed to $(1/\gamma_0^2)^{5/4}$. Using $r_0$, $\mathcal{E}_m(r_0)$, and $\gamma_0 \sim 2.5$ – the mean value in the range derived from BAT data – we find that $\mathcal{E}_m$ has been reduced by a factor of $\sim$0.026 to $\mathcal{E}_m \sim 0.3(1+z)$ keV $\sim 1.2$ keV. Our simulations show that the observed X-ray hardness ratio (Fig. 7) of $\sim 0.5 \pm 0.2$ just before the first flare is consistent with the reduced value of $\mathcal{E}_m$ mentioned above, only if the spectrum of the electrons also has steepened from $q \sim 3.5 \pm 0.5$ to $\sim$5. The steepness of this slope may signify the failure of the simplified model without an upper limit or high-energy break in the energy distribution of

[1] For simplicity in all the simulations discussed here we use a power law with constant index distribution for electrons.

[2] In all the calculations here we assume that the bulk Lorentz factor of the fireball $\gamma_{bulk} \gg 1$ and $\beta_{bulk} \sim 1$.

[3] Here we neglect the change in the bulk Lorentz factor. This happens mainly during the coalescence.

accelerated electrons. As mentioned above, this assumption is not realistic and can compromise the interpretation of the data.

The value we obtain for the decay index of the fields $\eta \sim 4$ is also slightly higher than its value after the steady-state regime during the main peak in the prompt gamma-ray emission $\eta \sim 3.5$. Both the increase in $\eta$ and electron distribution index $q$ are consistent with the cooling of the shell in this regime. What is remarkable is that we do not see a faster decay of the fields after the collision and coalescence of the shells both terminated. This means that the coherent bulk and field structures formed during the collision have relatively long lifetimes and do not disappear immediately after the end of collision.

Fig. 7 shows the hardness ratio of the X-ray bands for multiple flares detected by the XRT. The flare at $\sim T_0 + 98$ s was also observed by the BAT, and there is likely a small but delayed trace of it in the UVOT light curve, as explained in Section 3. A noticeable difference between the flare hardness ratio in the X-ray and the gamma-ray emission is that the hardness ratio of the X-ray flares follows, sometimes with lag or lead, the X-ray light curve, whereas, the hardness ratio of the gamma-ray emission, rises to a plateau and then declines slowly until the end of the spike.[4] A strong correlation is usually observed in flares where flares that brighten also harden (Goad et al. 2007a). This is interpreted as the consequence of the spectrum evolution and a decreasing break energy. However, in the case of GRB 060607a, a high-energy break was not observed in the XRT or BAT spectrum. Even without a break, the spectral evolution during a flare could still produce this correlation. None the less, rapid variation of the hardness ratio of flares in GRB 060607a does not seem to be a typical behaviour of all bursts, see e.g. the case for GRB 061121 (Page et al. 2007). One explanation could be a strong absorption of the soft-band photons which flatten the soft X-ray light curve. However, the flux hardness ratio curve in which corrections are made for the absorption has a very similar behaviour, and therefore absorption cannot be the cause. Another possibility is that the magnetic field and electron acceleration during the collision of the late shells with the remnant of the prompt shell did not achieve to rise to the steady-state regime and decayed exponentially once the late shell either coalesced with the prompt or passed through it. Our simulations also confirm this possibility.

As for the physical reasons for such behaviour, one important factor can be the heating of the prompt shell after its collision. It is well known (Waxman & Draine 2000; Wiersma & Achterberg 2004) that the development of a coherent magnetic and electron acceleration is weaker when the shock medium is hot and particles have a significant momentum in the direction perpendicular to the direction of the boost/bulk movement. As the hardness ratio in the flares does not seem to arrive to a steady-state regime, and we do not know the size and other characteristics of the late shells, we cannot estimate shock parameters for them as we did for the prompt gamma-ray peak. None the less, from our simulations using $q$ and $\eta$ similar to the prompt and continuous component of the X-ray light curve, we conclude that the shock is soft, consistent with weak or non-observation in the BAT bands.

[4] Note that we compare the behaviour of the X-ray hardness ratio of the main BAT peak with XRT flares. Although the first XRT flare of GRB 060607a was also observed by BAT, it is too weak to permit the calculation of a meaningful hardness. None the less, the similarity of the profiles in Fig. 8 suggests that the XRT hardness which is calculated for energy bands just less than one order of magnitude lower should most probably be a continuation of the same type of behaviour.

Like other bursts the most difficult part of the X-ray light curve to explain is the shallow slope regime. Various processes are suggested, such as, refreshed shocks by late shells (Rees & Mészáros 1998; Sari & Mészáros 2000), continuous energy injection to the fireball (prompt shell) (Yang et al. 1994; Dai & Lu 1998; Rees & Mészáros 2000), and variation of the microphysics of what remains from the prompt shell (Ioka et al. 2006). The first two processes seem to have an energy problem; they need much larger efficiency for gamma-ray emission than expected (Ioka et al. 2006). In addition, the uniform slope of this regime in all bursts does not look like a phenomenon relaying on the random injection of late/slow shells. The abrupt break at the end of this regime – especially in the case of GRB 060607A – needs a sudden stop of both energy injection and radiation that seems unphysical. By contrast, a change in the microphysics and energy dissipation of the prompt remnant and later shells seems a more reasonable cause. In fact, we see such a late time slow evolution of the intensities in the simulations. However, we do not see an abrupt break. Assuming that the late break in the X-ray light curve is not the jet break as it is not achromatic, its absence in simulations may be due to the limited precision of the numerical simulations and the simplicity of the model. Moreover, the fact that our analytical approximations are valid only for $\epsilon < 1$, and therefore, simulations are limited to this linear regime can be another factor influencing the lack of a break in the simulations. If this interpretation is correct, parameters of the shell are similar to the tail emission with a steeper slope. The X-ray hardness ratio is however higher than the tail emission see Fig. 7. Energy injection by flares to the prompt shell can be the reason for the hardening of the synchrotron emission. Another explanation can be the onset of a forward external shock by the ISM or circumburst material at a distance $\sim 10^{14}$ cm from the central engine.

The question which arises here is: At these late times, what keeps the coherent magnetic field and the electron acceleration in the shell going? Do we need a continuous fall of circumburst material or arrival of late shells (i.e. energy injection) to the shell to keep the radiation level high? Are the stock of electrons and residual magnetic field enough to keep the low flux of the late time radiation? In the first case either the circumburst material should exist at all distances after the prompt collision, or there must be a discontinuity in the emission between the end of the internal shock and the onset of the external forward shock. The same type of argument is relevant for the continuous energy injection. No discontinuity has been observed by *Swift*. Only a detailed knowledge of the origin of the ejecta, the shock, the state of the matter in the remnant after the prompt shock termination and the surrounding material can clarify these issues.

### 5.4 Modelling and interpretation of the UVOT data

Finally we try to explain the optical light curve of GRB 060607A which has interesting behaviour rarely seen in other bursts. In general, optical light curves of *Swift* bursts within the first few hundred seconds after the trigger, have a broad range of temporal indices, mostly consistent with decaying behaviour. After approximately 500s, all light curves are decaying (Oates et al., in preparation). In few bursts including GRB 060607A (see Figs 4 and 5), GRB 060418 (Molinari et al. 2007) and GRB 070616 (Starling et al. 2008) an initial rise in the optical light curves is detected in all filter from blue to infrared. A number of interpretations for this behaviour have been put forward: the onset of external shock (Nysewander et al. 2007), forward shock with ISM (Molinari et al. 2007), deceleration of the forward shock (Sari 1997) (Oates et al., in preparation). Here we argue that the most plausible reason for this behaviour is the gradual

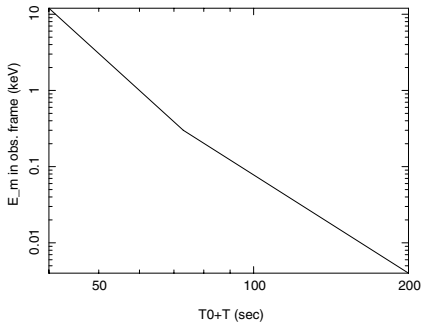


**Figure 9.** Estimation of the time evolution of $\mathcal{E}_{\rm m}$ in observer frame, from the end of the gamma-ray peak until the optical peak according to the model explained in Appendix A.

cooling and energy dissipation in the prompt shell and the entrance of $\mathcal{E}_{\rm m}$ to optical bands. The relatively shallow slope of the early X-ray light curve, $\alpha = 1.09$ may be the consequence of a slow evolution of $\mathcal{E}_{\rm m}$ which permitted the detection of its transition through the optical bands.

Using equation (4) and the argument about the evolution of $\gamma^2/\gamma_0^2$, we can estimate $\mathcal{E}_{\rm m}$ at the peak time in optical light curve $t_{\rm peak} \sim T_0 + 200/(z+1)$ s in the source rest frame, and we obtain $\mathcal{E}_{\rm m} \sim 4(1+z) = 16$ eV. This corresponds to ∼440 nm, with in the optical blue band for the observer. Therefore, we interpret the maximum of the light curve as the time where the characteristic synchrotron emission for the least energetic electrons enters to the optical bands. The approximate time evolution of $\mathcal{E}_{\rm m}$ according to the model used here is summarized in Fig. 9.

The rising slope of the optical light curve is $\alpha_{\rm opt}^{\rm rise} \sim 2.3 \pm 0.3$. According to the model, the slope in this regime is $q/2 - 1/6$. With the estimated $q \sim 5$ from the X-ray data, the observed value is consistent with the interpretation of the peak as the passage of $\mathcal{E}_{\rm m}$ to optical bands. Therefore, another component – external forward or reverse shock – is not required to explain the observations. Although there are UV observations for this burst, they do not begin until hundreds of seconds after the rise. Therefore it is not possible to see if they peak earlier than longer wavelengths, as would be expected from this interpretation. On the other hand, observations by the PROMPT telescope (Nysewander et al. 2007) in $B, g', r'$ and $i'$ are consistent with this interpretation. In fact the energy difference between $B$ and $i'$ bands with respect to the energy difference between X-ray and optical is very small, and therefore the expected time shift between their arrival to maximum is very small and difficult to detect with the time resolution of ground telescopes. Only UVOT in event mode could be able to directly detect the shift, but it cannot simultaneously observe with multiple filters. It may be possible to detect a small shift in the maximum by fitting the peak, but (Nysewander et al. 2007) did not attempt this. None the less, in fig. 1 of (Nysewander et al. 2007) which, includes the $H$-band data from the REM observations (Molinari et al. 2007), shows a small delay between the peak time in the $H$ band at $180 \pm 6$ s (Molinari et al. 2007) with respect to higher energy bands. We should also mention that flares observed in gamma- and X-ray bands are marginally distinguishable in the UVOT observations. This shows that as expected, the synchrotron emission from the flares is much harder than the cooling tail emission, and consequently no significant optical excess is observed during the X-ray flares. The lack of evidence for a significant external shock in the early low-energy bands emission makes the claim of determination of the bulk Lorentz factor (Molinari et al. 2007) unlikely, as it is based on the assumption that this peak is the result of a shock on the ISM. In this case $\gamma_{\rm bulk}$ is the same as collision $\gamma$ because ISM is roughly at rest with respect to the source. But according to our results the peak is related to the prompt shock and so the ISM/circumburst material had no significant contribution in its formation and properties.

The rest of the optical light curve follows a power-law decay at least until $\sim T_0 + 25\,000$ s without any change in the slope. The magnitude limits at later times are just brighter than the expected fluxes from a power-law decay and we cannot claim that any late break in optical/UV bands has been observed. The flattening or slight brightening from $\sim T_0 + 1000$ to $T_0 + 2000$ s (see Fig. 3) is probably related to the weak X-ray flare that occurred during this period.

Although the number of data points in the light curve in this regime is very limited, one can speculate that the slope of the decline is slightly steeper in longer wavelengths. This can be interpreted as the hardening of the emission, probably due to fireball encountering the ISM/circumburst material. In other words, it seems that a weak external shock starts a few thousands of seconds after the trigger and refreshes the prompt shell. Regarding just optical data, this claim seems very speculative. However, the hardness ratio of X-ray bands is definitely increasing (Fig. 7). This increases the hardness ratio to ∼1, i.e. $\mathcal{E}_{\rm m}$ moves to the X-ray band but with a smaller density for high-energy electrons. As the shell is already decelerated, a few thousands of seconds later at $\sim T_0 + 1.2 \times 10^4$ s the additional mass of the coalesced material from ISM breaks the coherence of the magnetic field and the synchrotron emission at higher energy bands begins a steep power-law decay due to a break in the spectrum of the electrons. This does not affect the emission in the optical bands from slower electrons. In this sense one can say that the X-ray and optical emissions come from separate components. It is also possible that at least part of the optical emission comes from the heated shocked material without the presence of a coherent magnetic field. In conclusion, the break is not likely to be associated with the jet break, i.e. when $1/\gamma_{\rm bulk} > \theta_{\rm jet}$, and the relativistic collimation is removed.

### 5.5 Alternative interpretations

To end the discussion, we consider some of the alternative interpretations of the optical light curves. First, we consider the possibility that the optical emission is produced by a forward or reverse external shock, and thus has a different origin than the prompt gamma-ray and the early X-ray emission. Considering first the forward shock case, the peak of the optical emission marks the onset of the afterglow where the peak time of the optical emission, $t_{\rm peak}$, is associated with the deceleration time of the outflow $t_{\rm dec}$, and with the optical emission at $t > t_{\rm dec}$, most likely dominated by the forward shock with $\mathcal{E}_{\rm opt} > \mathcal{E}_{\rm m}$. This conclusion is similar to the results we obtained by considering the early X-ray and optical emissions from the tail emission in the prompt shell without evoking a second component and a separate origin for the optical and X-ray emissions. In fact, using the observed power-law spectrum of the early X-ray, we can estimate the expected optical flux by extending the spectrum to the optical bands. What we find is summarized in Table 6. The observed magnitudes in this table are corrected for the Milky Way absorption which is only ∼0.1 mag. They are not corrected for the host absorption because we do not have any information about the dust-to-gas ratio in the host galaxy. As discussed in Section 4, the host of the most GRBs have values similar to SMC, $A_V \sim 1$ mag. Although the difference between the expected and the observed may partially be due to the absorption in the host, we also notice that discrepancies

**Table 6.** Expected and observed optical magnitudes in the $V$ band.

| Time + $T_0$ (s) | $V_{\rm pred}$ | $V_{\rm obs}$ | $\Delta\ V = V_{\rm obs} - V_{\rm pred}$ |
|---|---|---|---|
| 97 | 10.7 | 15.70 | 5.00 |
| 175 | 13.2 | 14.75 | 1.55 |
| 262 | 11.8 | 15.15 | 3.35 |

are time dependent, see Table 6. The value of $V_{\rm obs} - V_{\rm pred}$ varies from $\sim$1.5 to 5 mag depending on the time interval. The observational errors of the observed magnitudes are at most $\pm0.25$ at $1\sigma$ or $\pm0.5$ at $2\sigma$. They cannot explain the large variations as well as differences between expectations and observations. Therefore, we conclude that at least part of the difference between observations and expectations is intrinsic to the fireball. If the early X-ray and optical radiations have different origin, then the discrepancies between expectations and observations become even larger. This is because we must add the contribution in the optical flux of the other component to the contribution of the component producing the X-ray.

We now consider the possibility of a reverse shock as the source of the early optical emission. The rising slope of the optical light curve at $t < t_{\rm peak}$ is $\sim$2.3, which – in the context of the standard reverse shock model that predicts a slope of $\sim$1/3 – is too steep for the passage of $\mathcal{E}_{\rm m}$ through $\mathcal{E}_{\rm opt}$. The rising slope is a probe of the strength of the reverse shock and the observed slope suggests that the reverse shock is weak – the dimensionless parameter $\zeta \equiv \{[3E/(4\pi n m_{\rm p} c^2)]^{1/3}/\Delta r_0\}^{1/2}\ \Gamma^{-4/3}$ (Nakar & Piran 2004) presenting the strength of the reverse shock is large $\gtrsim$2. This lower limit on $\zeta$ is valid both if the emission at $t < t_{\rm peak}$ is dominated by the forward external shock or if it is from a non-relativistic or at most mildly relativistic reverse shock (Nakar & Piran 2004). Therefore, it seems that for this burst the contributions of these components are small. None the less, if the early optical emission is due to a reverse shock, the temporal slope of the rising phase also probes the external density profile. A wind-like density profile would produce a significantly slower rise than a uniform external density. The steep rise seems to favour a uniform external density over a wind-like density profile below and around the deceleration radius $r_{\rm dec}$. More specifically, a wind-like external density profile could not produce such a sharp rise either by a forward or through a reverse shock even if the reverse shock is extremely weak ($\zeta \gg 1$) and the outflow acts as a perfect piston as far as the external medium is concerned.

Another possible explanation is that the optical emission is mainly produced by the combination of reverse shock and energy injection. The latter is one of the possible causes for the slow decay of the optical light curve after the peak $\sim t^{-1.3}$ compared to the $\sim t^{-2}$ expected for an idealized reverse shock where the outflow has a sharp lower cut-off in $\gamma$. The observation of X-ray flares for this burst is also consistent with the additional outflow after the prompt shell.

There is a minor break in the optical light (seen more clearly in the data of Molinari et al. 2007) at $\sim T_0 + 103$ s, roughly at the end of the bright X-ray flares and before the small X-ray/optical flare. This may be the evidence of the break in the reverse shock after a relatively flat regime following the initial rise (Zhang & Mészáros 2002). However, for this argument to be viable, the reverse shock should be significantly brighter than the forward shock. Regarding the arguments above about the weakness of the reverse shock, it does not seem that we can associate this break to the reverse shock.

We should also mention that the above break can be also explained as a hardening of the radiation at the arrival of a new shell responsible for the weak flare in XRT data (see Fig. 2) at $\sim T_0 + 1260$ s. A similar break is also visible in the UVOT light curve during the flare at $\sim T_0 + 260$ s, followed by a slightly steeper fall of the optical light curve most probably due to energy injection and hardening of the emission (see Fig. 4). Therefore, considering all the arguments together, the evidence for a dominant reverse shock is weak.

## 6 CONCLUSION

After years of investigation and especially with the multiband data from *Swift* of more than 200 bursts, it is clear that complex physical processes are involved not only in the physics of the progenitor but also in the collisions between ejected material and the surroundings that at first sight seem simple.

In this work we applied the internal/external shock model as the source of observed emission to GRB 060607A, one of the most peculiar GRBs observed by *Swift*. We tried to understand and interpret the acquired data and related processes partly qualitatively, partly quantitatively. We estimated the distance to the central engine where the collisions between shells occurred to be $\sim 10^{12}$ cm. This is consistent with the original suggestion of the model in which, internal shocks happen at a distance of $r \sim 10^{11}$–$10^{13}$ cm from the central engine. We also found that the external shocks influence the afterglow of this burst only at late times; most probably a few thousand seconds after the prompt emission. If our interpretations are correct, it seems that the coherent magnetic field in the fireball can have relatively long lifetime and the energy distribution of electrons can be much more complex than a simple power law. Based on the hardness ratio in the X-ray band we showed that there is a separation between population/sources of electrons responsible for the late X-ray and optical emission. In particular we conjectured the presence of a non-synchrotron, close to thermal component in the optical emission from the shocked heated material at late times in the afterglow of GRBs. The measurement of the late time optical spectrum can verify this hypothesis. A better understanding of the relativistic plasma physics is also necessary and will provide realistic models for the evolution of fields and charged particles acceleration and energy distribution during the shock and their relation with the state of matter in the ejecta (fireball).

## ACKNOWLEDGMENTS

This research has made use of data obtained through the High Energy Astrophysics Science Archive Research Center Online Service, provided by NASA's Goddard Space Flight Center.

## REFERENCES

Achterberg A., Gallant Y. A., Kirk J. G., Guthmann A. W., 2001, MNRAS, 328, 393
Akerlof C. et al., 1999, Nat, 398, 400
Akerlof C. W. et al., 2003, PASP, 115, 132
Amano T., Hoshino M., 2007, ApJ, 661, 190
Arnaud K. A., 1996, in Jacoby G., Barnes J., eds, ASP Conf. Ser., Vol. 101, Astronomical Data Analysis Software and Systems V. Astron. Soc. Pac., San Francisco, p. 17
Barthelmy S. D. et al., 2005, Space Sci. Rev., 120, 143
Bednarz J., Ostrowski M., 1996, MNRAS, 283, 447
Boër M., 2001, Astron. Nachr., 322, 343
Burrows D. N. et al., 2005, Space Sci. Rev., 120, 165
Butler N. R. et al., 2006, ApJ, 652, 1390
Covino S. et al., 2004, in Moorwood A. F. M., Masanori I., Proc. SPIE Vol. 5492, Ground-based Instrumentation for Astronomy. SPIE, Bellingham, p. 1613

Dai Z. G., Lu T., 1998, A&A, 333, L87
Dai X., Halpern J. P., Morgan N. D., Armstrong E., Mirabal N., Haislip J. B., Reichart D. E., Stanek K. Z., 2007, ApJ, 658, 509
Fenimore E. E., in't Zand J. J. M., Norris J. P., Bonnel J. T., Nemiroff R. J., 1995, ApJ, 101, L448
Fenimore E. E., Madras C. D., Nayakshin S., 1996, ApJ, 473, 998
Frail D. A. et al., 2001, ApJ, 562, L55
Fynbo J. P. U. et al., 2001, A&A, 373, 796
Gehrels N. et al., 2004, ApJ, 611, 1005
Goad M. et al., 2007a, A&A, 468, 103
Goad M. et al., 2007b, A&A, 476, 1401
Hjorth J. et al., 2003, ApJ, 597, 699
Holland S. T. et al., 2007, AJ, 133, 12
Ioka K., Toma K., Yamazaki R., Nakamura T., 2006, A&A, 458, 71
Jackson J. D., 1999, Classical Electrodynamics, 3rd edn. Wiley, New York
Jensen B. L., Fynbo J. P. U., Gorosabel J., Hjorth J., Holland S. T., Møller P., Thomsen B., Björnsson G., 2001, A&A, 370, 909
Kann D. A., Klose S., Zeh A., 2006, ApJ, 641, 993
Kirk J. G., Guthmann A. W., Gallant Y. A., Achterberg A., 2000, ApJ, 542, 235
Kumar P. et al., 2007, MNRAS, 376, L75
Ledoux C., Vreeswijk P., Smette A., Jaunsen A., Kaufer A., 2006, GCN Circ., 5237
Liang E. W. et al., 2006, ApJ, 646, 351
Misra K., Bhattacharya D., Sahu D. K., Sagar R., Anupama G. C., Castro-Tirado A. J., Guziy S. S., Bhatt B. C., 2007, A&A, 464, 903
Molinari E. et al., 2007, A&A, 469, L13
Nakar E., Piran T., 2002, MNRAS, 331, 40
Nakar E., Piran T., 2004, MNRAS, 353, 647
Nousek J. A. et al., 2006, ApJ, 642, 389
Nysewander M., Haislip J., 2006, GCN Circ., 5236
Nysewander M., Reichart D. E., Crain J. A., Foster A., Haislip J., Ivarsen K., Lacluyze A. J., Trotter A., 2007, ApJ, submitted (arXiv:0708.3444)
Oates S. R., Blustin A. J., Ziaeepour H., 2006, GCN Circ., 5243
O'Brien P. T. et al., 2006, ApJ, 647, 1213
Page K., Goad M., Beardmore A., 2006, GCN Circ., 5240
Page K. L. et al., 2007, ApJ, 663, 1125
Pei Y., 1992, ApJ, 395, 130
Perna R., Lazzati D., Fiore F., 2003, ApJ, 585, 775
P'erez-Ramírez D., Merlioni A., Rees M. J., 2004, Astron. Nachr., 324, 1147
Predehl P., Schmitt J. H. M. M., 1995, A&A, 293, 889
Ramirez-Ruiz E. F., Merloni A., 2001, MNRAS, 320, L25
Ramirez-Ruiz E. F., Merloni A., Rees M. J., 2001, MNRAS, 324, 1147
Rees M. J., Mészáros P., 1994, ApJ, 430, L93
Rees M. J., Mészáros P., 1998, ApJ, 496, L1
Rees M. J., Mészáros P., 2000, ApJ, 545, L73
Reville B., Kirk J. G., Duffy P., 2006, Comments Plasma Phys. Control. Fusion, 48, 1741
Rhoads J. E., 1999, ApJ, 525, 737
Rieger F. M., Bosch-Ramon V., Duffy P., 2007, Ap&SS, 309, 119
Romano P. et al., 2006, A&A, 456, 917
Roming P. W. A. et al., 2005, Space Sci. Rev., 120, 95
Sari R., 1997, ApJ, 489, L37
Sari R., Mészáros P., 2000, ApJ, 535, L33
Sari R., Narayan R., Piran T., 1996, ApJ, 473, 204
Sari R., Piran T., Narayan R., 1998, ApJ, 497, L17
Sari R., Piran T., Halpern J. P., 1999, ApJ, 519, L17
Savitzky A., Golay M. J. E., 1964, Anal. Chem., 36, 1627
Schady P. et al., 2007a, MNRAS, 377, 273
Schady P. et al., 2007b, MNRAS, 380, 1041
Schlegel D. J., Finkbeiner D. P., Davis M., 1998, ApJ, 500, 525
Shen R., Kumar P., Robinson E. L., 2006, MNRAS, 371, 1441
Starling R. L. C. et al., 2007, GCN Circ., 6542
Starling R. L. C. et al. 2008, MNRAS, 384, 504
Stamatikos M. et al., 2007, GCN Rep., 25.1
Stratta G., Fiore F., Antonelli L. A., De Pasquale M., 2004, ApJ, 608, 846
Tueller J. et al., 2006, GCN Circ., 5242
Vestrand W .T. et al., 2002, in Kibrick R. I., ed., Proc. SPIE Vol. 4845, Advanced Global Communications Technologies for Astronomy II. SPIE, Bellingham, p. 126
Vestrand W. T. et al., 2005, Nat, 435, 178
Vestrand W. T. et al., 2005, Nat, 442, 172
Watson D., Hjorth J., Fynbo J. P. U., Jakobsson P., Foley S., Sollerman J., Wijers R. A. M. J., 2007, ApJ, 660, 101
Waxman E., Draine B. T., 2000, ApJ, 537, 796
Wei D. M., Lu T., 2002, MNRAS, 332, 994
Wiersma J., Achterberg A., 2004, A&A, 428, 365
Willingale R. et al., 2007, ApJ, 662, 1093
Yang T. Y. B., Arons J., Langdon A. B., 1994, Phys. Plasma, 1, 3059
Yost S. A. et al., 2007, ApJ, 657, 925
Zhang B., Mészaros P., 2002, ApJ, 566, 712
Zhang B., Kobayashi S., 2005, ApJ, 628, 315
Zhang B., Fan Y. Z., Dyks J., Kobayashi S., Mészáros P., Burrows D. N., Nousek J. A., Gehrels N., 2006, ApJ, 642, 354
Zhang B. B., Liang E. N., Zhang B., 2007, ApJ, 666, 1002
Ziaeepour H. et al., 2006, GCN Circ., 5233

## APPENDIX A: A RELATIVISTIC SHOCK MODEL WITH ONE ACTIVE REGION

In this appendix we briefly review the main aspects and results of the shock model used for comparison with data. It is a reformulation of the relativistic shock models with only one synchrotron emitting shocked layer but more detailed parametrization of the physical processes and their time variation (Ziaeepour, in preparation).

We consider a radiative shock between two relativistic spherical shells. For an observer in the rest frame of the fast shell, the kinetic energy of the falling particles from the slow shell is instantaneously emitted as the shells join and merge together. A far observer sees that the fast shell absorbs the slow one, its density and/or size increases and its Lorentz factor decreases. During coalescence, we distinguish one region of unshocked material in each shell, and one shocked zone in which charged particles are accelerated by the coherent electric field produced be the shock. In presence of a coherent magnetic field, these charged particles irradiate their energy as synchrotron radiation. The magnetic field is usually considered to be produced by the shock as well (Yang et al. 1994; Wiersma & Achterberg 2004). It is also possible that there is an additional ambient magnetic field produced by the central engine. Here we neglect this possibility. This model is a simplified version of the relativistic shock model (Sari, Narayan & Piran 1996) that considers one shocked region in each side of the shock discontinuity – forward and reverse. The lack of a clear evidence for a reverse shock emission in any burst, specially during the prompt emission, means that the reverse shock in GRBs is weak and the assumption of just one shocked region is a good approximation.

Energy–momentum conservation equations in the slow shell/ISM frame is

$$\gamma\left(r^2\frac{\mathrm{d}(n\Delta r)}{\mathrm{d}r}+2r(n\Delta r)\right)+r^2(n\Delta r)\frac{\mathrm{d}\gamma}{\mathrm{d}r} = n_0\gamma r^2+\frac{\mathrm{d}E_{\mathrm{sy}}}{4\pi mc^2\,\mathrm{d}r} \tag{A1}$$

$$\beta\gamma\left(r^2\frac{\mathrm{d}(n\Delta r)}{\mathrm{d}r}+2r(n\Delta r)\right)+r^2(n\Delta r)\,\mathrm{d}(\beta\gamma) = n_0\beta\gamma r^2+\frac{\mathrm{d}E_{\mathrm{sy}}}{4\pi mc^2\,\mathrm{d}r}, \tag{A2}$$

where $r$ is the distance from the central engine, $n$ is the number density of the fast shell measured in the slow shell frame,

$n_0$ is the number density of the slow shell in its rest frame, $\Delta r$ is the thickness of the shocked synchrotron emitting region, $\gamma$ is the Lorentz factor of the fast shell in the slow shell frame and $\beta = \sqrt{\gamma^2 - 1}/\gamma$, $m = m_\mathrm{p} + m_\mathrm{e} \approx m_\mathrm{p}$, $E_\mathrm{sy}$ is the total emitted energy and $c$ is the speed of light. In the absence of knowledge about the evolution of microphysics of the shocked region, we cannot evaluate the evolution of $\Delta r$. However, the left-hand side of equations (A1) and (A2) depends on $n\Delta r$ – the column density of shocked region.

The total power of synchrotron emission depends on the number of emitters. If only falling electrons are accelerated, the number of emitting sources are proportional to $n_0$. In this case we have to consider a model for the evolution of the shocked region. A minimal estimation is $\Delta r = \beta\, \Delta r_0/\gamma$ where $\Delta r_0$ is a constant thickness scale. The physical reason for this choice is that in the two extreme cases when the relative Lorentz factor is very large or very small, one expects a thin shocked region. In the first case the reason is that due to the large density difference between shells only a thin layer of the fast shell is affected (shocked) be the falling particles from slow shell. In the second case the shock is soft, the two shells merge smoothly and one expects that the size of the turbulent shocked particles be very restricted. Another plausible model is the acceleration of all the electrons in the shocked region following the formation of a coherent electric field in the shock. In this case, the column density of emitters is proportional to $n\Delta r$, and therefore an ad hoc expression for the evolution of $\Delta r$ is not needed. Both these cases are based on the assumptions that only a detail knowledge about the microphysics of the matter state and shock can confirm or role out. None the less, if the rest frame densities of the shells are close to each other, these approximations should give similar results. For simplicity, here we will consider the first case which makes the right-hand side of (A1) and (A2) independent of $n$.

We expect that $\Delta r/r \ll 1$ although in some circumstances the thickness of the shells can be comparable with $r$. If $r \to \infty$, the shells become planar. If the shells are not spherical but collimated, the formulation of the shock and synchrotron radiation is more complex. However, it can be shown that at first approximation, the total flux can be considered as proportional to the opening angle of the jet. Hence for simplicity we do not discuss the effect of the collimation further here.

Variation of the synchrotron energy can be related to the emission power $\mathrm{d}E_\mathrm{sy}/\mathrm{d}r = \mathrm{d}E_\mathrm{sy}/\beta\, \mathrm{d}t = P_\mathrm{sy}/\beta$, where $P_\mathrm{sy}$ is the total power of the synchrotron emission. Assuming a power-law distribution for the Lorentz factor of the accelerated electrons, $\mathrm{d}E_\mathrm{sy}/\mathrm{d}r$ can be written as a function of the relative Lorentz factor $\gamma$, $\epsilon_\mathrm{e}$, $\epsilon_B$ and $q$,[5] respectively, the fraction of kinetic energy of the shell transferred to accelerated electrons, the fraction of kinetic energy transferred to a coherent magnetic field, and the number distribution index of accelerated electrons (Sari, Piran & Narayan 1998). We assume that $q$ is a constant but $\epsilon_\mathrm{e}$, $\epsilon_B$ have power-law dependence on $r$ with indices $\alpha_\mathrm{e}$ and $\alpha_B$, respectively. Then we can solve equations (A1) and (A2) to find the evolution of $\gamma$ and the column density of synchrotron emitting layer $n\Delta r$. These equations are coupled and therefore some approximations are necessary to decouple and solve them. In addition, their solutions depend on the relative strength of the various parameters.

At the lowest order in $\epsilon$, and when $r/r_0 - 1 \ll 1$, the evolution of $\gamma$ can be expressed in the following form:

$$\frac{\gamma^2(r)}{\gamma^2(r_0)} = \frac{1}{1 + F\epsilon + \cdots}, \quad \frac{r}{r_0} \equiv 1 + \epsilon, \quad \epsilon \ll 1. \tag{A3}$$

The coefficient $F$ depends on various physical quantities such as initial relative Lorentz factor of the colliding shells, their initial densities, $\epsilon_\mathrm{e}, \epsilon_B$, the number distribution index of accelerated electrons $q$ and the variation of these quantities with time. They are degenerate and the extraction of all of them from available data is not possible.

The column density of synchrotron emitting layer at the lowest order and with approximations mentioned above is

$$\frac{n\Delta r}{n(r_0)\Delta r_0} = \left(\frac{r_0^2}{r^2}\right)\left[1 + F_1\left(\frac{r_0^2}{r^2}\right)^{\alpha'} + \cdots\right], \tag{A4}$$

where the term $r_0^2/r^2$ is simply due to the adiabatic expansion of the shell. The constant $F_1$ depends on various parameters mentioned about. The exponent $\alpha'$ consists of two parts: a constant and a part dependent on $\eta \equiv 2\alpha_\mathrm{e} + \alpha_B$. This shows the importance of the evolution of coherent electric and magnetic fields in the GRBs.

Evidently, the only observable outcome of the shell collision for us is the synchrotron emission. Its intensity for one charged particle is well known (Jackson 1999), and in order to obtain the total intensity we should integrate it over the emitting volume and the spectrum of the synchrotron emitting charged particles (electrons):

$$\frac{\mathrm{d}I}{\mathrm{d}\nu} = 2\sqrt{3}\pi\frac{e^2}{c}V(r)\gamma\int_\Gamma^\infty \mathrm{d}\gamma_\mathrm{e} n_\mathrm{e}(\gamma_\mathrm{e})\frac{\nu}{\nu_\mathrm{c}}\int_{\nu/\nu_\mathrm{c}}^\infty K_{5/3}(x)\,\mathrm{d}x, \tag{A5}$$

where $V(r)$ is the volume of the synchrotron emitting layer, $\nu_\mathrm{c}$ is synchrotron characteristic frequency, $n_\mathrm{e}(\gamma_\mathrm{e})$ is the electron density with Lorentz factor $\gamma_\mathrm{e}$, $\Gamma$ is the minimum Lorentz factor of the accelerated electrons and finally $K_{5/3}$ is the Bessel function. Although $\frac{\mathrm{d}I}{\mathrm{d}\nu}$ is the main observable quantity, it depends on too many unknown parameters and in practice it cannot be efficiently used. Two other quantities derived from intensity are more useful. One is the hardness ratio and the other is the lag of the peak emission in different energy bands:

$$\mathrm{HR}_{ij} \equiv \frac{\bar\nu_i(\mathrm{d}I/\mathrm{d}\bar\nu_i)\log\left(\nu_i^\mathrm{max}/\nu_i^\mathrm{min}\right)}{\bar\nu_j(\mathrm{d}I/\mathrm{d}\bar\nu_j)\log\left(\nu_j^\mathrm{max}/\nu_j^\mathrm{min}\right)}, \tag{A6}$$

$$\Delta\epsilon_{ij} = \epsilon_i^\mathrm{peak} - \epsilon_j^\mathrm{peak}, \quad \frac{\mathrm{d}}{\mathrm{d}\epsilon}\left(\frac{\mathrm{d}I}{\mathrm{d}\nu}\right)\bigg|_{\epsilon^\mathrm{peak}} = 0, \tag{A7}$$

where $i$ and $j$ are different energy bands with logarithmic mean frequency $\bar\nu$ and minimum and maximum frequency $\nu^\mathrm{min}$ and $\nu^\mathrm{max}$, respectively. The variable $\epsilon$ is defined in equation (A3). The hardness ratio can be determined directly from the data for all energy bands. However, the lags are only measurable for fast-varying features such gamma-ray peaks and X-ray flares. None the less, when they are measurable they give valuable information about the distance to the central engine at which, the corresponding events have occurred. Note that $\epsilon_i$ and $\epsilon_j$ in (A7) are dimensionless relative quantities. However, the measured lags are not. Therefore, if the lags in multiple bands are available, we can estimate the value of the corresponding $\epsilon$ values thereby we can measure the initial distance $r_0$.

It can be shown that $\mathrm{HR}_{ij}$ and $\Delta\epsilon_{ij}$ depend on $r$ (or equivalently $t$ or $\epsilon$) through the function $C(r, \nu) \equiv \nu/\nu_\mathrm{c}'\Gamma^2 = \nu/\nu_\mathrm{m}$, where $\nu_\mathrm{c}' \equiv eB/m_\mathrm{e}c$ depends only on the magnetic field. Therefore, even without any knowledge about other quantities, the evolution of the hardness ratio directly shows the evolution of $\nu_\mathrm{m}$. The analytical expression for $\mathrm{HR}_{ij}$ and specially for $\Delta\epsilon_{ij}$ are quite involved. Moreover, the

[5] The more popular parameter $p$ the energy distribution index of the accelerated electrons is related to $q$: $p = q - 1$.

integral over the Bessel function in (A5) must be calculated numerically. Our experience shows that the use of asymptotic values of the Bessel function which permit to obtain analytical expressions for these quantities leads to large errors and unphysical behaviour of the results. The results of numerical calculation for a number of combination of parameters will be reported in Ziaeepour (in preparation) and we have used them for analysing GRB 060607A data.

## APPENDIX B: EXTRAPOLATION OF BAT AND XRT SPECTRA

Practically in all GRBs the spectrum becomes softer after the end of the main prompt spikes. Therefore the spectral index of the gamma-ray spectrum should be considered as a slowly time-varying quantity. The total X-ray flux $f_{\gamma-X}(t)$ expected is approximately

$$f_{\gamma-X}(t) \approx \frac{f_\gamma(t)}{E_{\max}-E_{\min}} \int_{E_{\min}}^{E_{\max}} \left(\frac{E_X}{\bar{E}_\gamma}\right)^{\alpha_\gamma(t)} \mathrm{d}E_X \approx \frac{f_\gamma(t)}{\alpha_\gamma(t)+1} \left(\frac{E_{\max}}{\bar{E}_\gamma}\right)^{\alpha_\gamma(t)}, \quad \text{(B1)}$$

where $\bar{E}_\gamma$ is the logarithmic mean of gamma-ray energy band, $E_{\max}$ and $E_{\min}$ are maximum and minimum of the X-ray energy band and $\alpha_\gamma(t)$ is the slowly varying spectral index.

In the method explained in Section 4 for the extrapolation of BAT spectrum to X-ray band, a simple average of the spectral index, usually from the total BAT spectrum and early X-ray spectrum is used as an approximation to take into account the time evolution of the spectrum. Using the same formulation as in equation (B1), the extrapolated BAT light curve to the XRT band $f_{\mathrm{BAT-XRT}}(t)$ can be estimated as

$$f_{\text{BAT-XRT}}(t) \approx \frac{N f_{\mathrm{BAT}}(t)}{\bar{\alpha}(t)+1} \left(\frac{E_{\max}}{\bar{E}_\gamma}\right)^{\bar{\alpha}}, \quad \text{(B2)}$$

where $\bar{\alpha}$ is the average of BAT and XRT spectrum indices and $N$ is a normalization factor between the two instruments. In general, the cruder approximation of (B2) will not agree with the more precise expression (B1) unless $\alpha_\gamma(t)$ have roughly a linear and slow evolution with time. If these conditions are not fulfilled and/or the prompt and the tail emission in X-ray have different origins, the extrapolated light curve (B2) should deviate from the observed one, or a break appears when one tries to join simultaneous observations by BAT and XRT. This break cannot be removed by adjusting the normalization factor $N$ in (B2). Among 40 *Swift* GRBs studied in (O'Brien et al. 2006) only a few of them seems to need such a break to join the extrapolated BAT and the observed XRT light curves: GRB 050315, GRB 050713B and GRB 050915B. In conclusion, (B2) is a good approximation of (B1) for most bursts and when it is not, the probability of having a smooth and overlapping light curve with the XRT observations is very small.

This paper has been typeset from a TEX/LATEX file prepared by the author.